Photocatalytic and structure evaluation of g-C_3N_4/carbon microspheres and melam/dimelem intermediates under white LED and UVA-Vis irradiation

Adriana Patricia Rodríguez-Pérez[1], Rhaissa Dayane Carneiro de Christan[1], Rafaela Imoski[1], Laís Jarenko da Cruz[1], Breidi Albach[2], Carla Dalmolin[3], Daniel da Silveira Rampon[4], Cristian Santacruz[5], Farooq Sher[6], Wanessa Algarte Ramsdorf[1], Liziê Daniela Tentler Prola[1,7,*] and Marcus Vinicius de Liz[1]

[1] *Research Group on Water and Wastewater Advanced Treatment Technologies (GPTec), Department of Chemistry and Biology, The Federal University of Technology-Paraná (UTFPR), Deputado Heitor de Alencar Furtado St., 5000, Ecoville, 81280-340 Curitiba, Paraná, Brazil*

[2] *Health Department, Unicesumar - University Center of Maringá, Curitiba, PR, 81070-190, Brazil*

[3] *Department of Chemistry, Santa Catarina State University (UDESC), Av. Me. Benvenuta, 2007 - Itacorubi, Florianópolis - SC, Brasil, 88035-001*

[4] *Laboratory of Polymers and Catalysis (LaPoCa), Department of Chemistry, Federal University of Parana (UFPR), 81531-990, P.O. Box 190*

[5] *Departamento de Física, Escuela Politécnica Nacional, Ladrón de Guevara E11-253, Quito – Ecuador*

[6] *Department of Engineering, School of Science and Technology, Nottingham Trent University, Nottingham NG11 8NS, United Kingdom*

[7] *International Society of Engineering Science and Technology, Nottingham, United Kingdom*

Abstract

Despite the polymeric metal-free graphitic carbon nitride (g-C_3N_4) has been extensively studied for photodegradation, intermediate oligomers (melam/dimelem) can be generated during the polymerization process and it is a subject matter. The melem compounds feature active amino groups (-NH_2) partially linked to one another, facilitating intermolecular reactions and alteration of the compound's structure. This study evaluated the synergic effect of carbon matrix on the physicochemical and electronic characteristics of g-C_3N_4 (CN) and melam/dimelem intermediates compounds by synthesis *in situ* of chitosan and CN precursors. The g-C_3N_4 were obtained using urea (U) and melamine (M), denoted as CN/U and CN/M, and the carbon microspheres, denoted as CN/CU and CN/CM. The characterizations suggest C−N sp^2-hybridized bonds between the carbon ring from chitosan and the melam/dimelem unit, which may be highly activated either in the visible or UVA regions. An increase of 16% in photocatalytic efficiency for CN/CM material was observed by incorporating chitosan in the g-C_3N_4 using LED light. The carbon microspheres interact synergistically with the bulk g-C_3N_4 to form two-dimensional planes in which the charge carriers can move freely along the carbon ring structure. The carbon microspheres are an excellent option to separate the photocatalyst easily from the reaction mixture. Additionally, the photocatalytic degradation mechanism of RhB by carbon microspheres was also proposed.

Keywords: synergic effect, synthesis *in situ*, visible-light, RhB, metal-free

1 Introduction

According to the United Nations Report on World Water Resources, roughly 80% of the wastewater steam is discharged into the environment without any treatment. As a result, a broad portion of the water bodies has been contaminated, resulting in adverse effects on aquatic organisms and human health [1]. Among water treatments [2,3], photocatalysis is an effective alternative to removing contaminants from wastewater that can reduce pollutants to CO_2 and H_2O to harmless substances [4,5]. Recently, a new metal-free graphitic carbon nitride (g-C_3N_4) has received attention due to its visible-light responsiveness and effective solar spectrum utilization for photocatalysis and wastewater pollution [6,7]. g-C_3N_4 (CN) is two-dimensional conjugated inorganic polymeric material with a graphite-like structure interconnected tri-s-triazine by units through nitrogen tri-s-triazine/planar amino groups. The material has a π-conjugated structure with a narrow band gap (2.7 eV), leading to optical absorption in the visible region up to 460 nm [8,9].

Besides, it is facile synthesized by thermal polycondensation from abundant nitrogen-rich precursors such as urea, melamine, and thiourea, among others [8,10]. However, during carbon nitride-based synthesis, intermediates with photocatalytic properties in the UV region, such as melam and dimelem could be formed by incomplete carbonization [11]. These compounds are dominated by π–π interactions and lateral hydrogen bonds resulting in the arrangement of molecules to generate an ordered molecular crystal and strong absorption peak in the UV-Vis spectrum, corresponding to a blue-shifted absorption compared to g-C_3N_4 [11]. Despite the extensive research about g-C_3N_4 material, there are few studies regarding the structure, photoactivity and synthesis of melem derivatives [12,13]. Hence, an emerging need for studies related to these compounds.

Several synthesis strategies have been explored to improve the g-C_3N_4 photocatalytic properties based on membrane technology [14], metal and non-metal doping [15–17],

anion doping [18], heterojunction based on metal-oxides [19], surface modification by controlling morphology [20], coupling with semiconductors [21] and dye-sensitization [22].

Natural precursors such as waste carbon materials have been used to design new hybrid materials. The in-plane π-conjugated C-ring bonds synergistically extend the light absorption and promote the photogenerated charge separation and transportation of CN and derivatives [23,24]. In fact, most studies of g-C_3N_4 carbon functionalized methods involve two or more steps of synthesis separately: (i) thermal polycondensation of CN precursor followed by (ii) incorporation of carbon material in the CN matrix [21]. To our knowledge, few studies have combined *situ* g-C_3N_4 and carbon precursors.

For instance, Djoko et al. [24] synthesized CN/carbon nanocomposites by thermal condensation of green tea leaves and melamine. Xu et al. [23] Obtained amorphous carbon/CN composites through one-step thermal using glucose and urea as precursors [23].

Xenon lamp [25–27] is the predominant photo-irradiation source used to evaluate materials' photoactivity with few reports regarding the use of white LED [28,29] and UVA irradiation [29,30]. Visible LEDs consume relatively low electrical power, high life, and less heat than conventional light sources (tungsten and xenon) and emit around 400 nm, making them promising for photocatalysis studies. Di et al. [31] investigated the wavelength and intensity effect on quantum dots (CQDs)/g-C_3N_4 carbon photocatalyst using LED with light emission ranging from 395 to 500 nm. Under different excitation wavelengths, the CQDs exerted differentiated effects on g-C_3N_4. Furthermore, 395 and 455 nm wavelengths exhibit a linear dependence between degradation rate and radiation intensity [31].

Recovery, reusability, and stability are also subject to research to separate photocatalyst from aqueous solution [21]. Powder semiconductors tend to agglomerate during the

reactions loading hinders light penetration, which influences photocatalytic rates [32]. Notably, Spherical carbon structures as template for semiconductor is an effective method for material stability and recovery from the solution phase [33–35].

We propose a new metal-free structures approach by investigating their interaction with light and the carbon matrix synergistic effect on g-C_3N_4 and its intermediates. This work focuses on a novel and effective method for producing *in situ* carbon microspheres and metal-free melem derivatives via thermal condensation of urea, melamine precursors, and chitosan, which is a biodegradable, non-toxic, cheap, and abundant polymeric material. The photocatalytic mechanism and efficiency were discussed based on the carbon matrix effect on the g-C_3N_4 and melam derivatives under white LED and UVA-Vis irradiation. Besides, we studied the properties of the materials and photocatalytic performance through phase, morphology, optical properties, and chemical composition characterization. The stability and recyclability of carbon microspheres and carbon nitride materials were also investigated.

2 Experimental

2.1 Chemicals and reagents

All chemicals used in this study were used without further purification. Urea (CH_4N_2O, ≥ 99 %, Merck), melamine ($C_3H_6N_6$, ≥ 99 %, Sigma-Aldrich), Rhodamine B (RhB, CAS 81889, Dinâmica), chitosan (degree of deacetylation ≥ 95%, Galena), Acetic acid (ALPHATEC) and glutaraldehyde (50 % w/v). The deionized water from Milli-Q system (Millipore, Bedford, MA, USA) was used in all the experiments.

2.2 Synthesis of CN samples and CN/C carbon microspheres

The g-C_3N_4 (CN) products were synthesized by directly heating urea (U) or melamine (M) in a closed crucible according to the previously described literature [8,27]. Typically, 10 g

of melamine or urea was placed into a sealed crucible and subsequently heated at 550 °C for 2 h at rate 5 °C min^{-1}. The resultant yellow material was naturally cooled down and grounded into a fine powder and denoted as CN/U and CN/M for urea and melamine, respectively. The g-C_3N_4/carbon microspheres (CN/C) were synthesized by a facile method, according to Prola et al. [36]. A homogenous mixture of 1 g urea (U) or melamine (M) and 3 g chitosan (CS) in acetic acid (HAc, 80 mL, 5% v/v) was dropwise into sodium hydroxide (2 mol L^{-1}) solution. The microspheres were washed and crosslinked with an aqueous glutaraldehyde solution (1% v/v) for 17 h. The microspheres were placed into a sealed crucible and heated at 550 °C for 2 h in a muffle furnace at a rate 5 °C min^{-1} (**Fig. S1**). The materials were denoted as CN/CU and CN/CM for urea and melamine, respectively.

2.3 Photocatalysis experiments

The materials' photocatalytic efficiency was evaluated under UVA-Vis and visible radiation at neutral pH and 30 mg of the photocatalyst. For UVA-Vis radiation was used a 125 W high-pressure mercury vapor lamp (without its original bulb) and covered with a Pyrex bulb (315–800 nm) immersed into the borosilicate bench-scale reactor (300 mL) with water recirculation at 25 °C. For visible radiation, a LED lamp (50W, λ=420–715 nm) was suspended 10 cm from the surface of the Pyrex reactor (300 mL) and external cooling (**Fig. S2**). To achieve adsorption-desorption equilibrium, the solution contained the photocatalyst and the RhB (10 mg L^{-1}) was magnetically for 15 min in the dark and then irradiated for 60 min. Thus, aliquots (2 mL) were collected at pre-determined intervals and filtered through a 0.47 μm glass fiber filter (MN GF-3). The carbon microspheres could easily be removed from the solution.

2.4 Samples characterization

The Rhodamine B (RhB) quantification was performed using a UV-Vis spectrometer Carry Bio (VARIAN) at a wavelength of 555 nm. The morphology of the materials was characterized using an EVO MA 15 (Zeiss) scanning electron microscope. The AFM study was using an atomic force microscope SPM-9700 HT (Shimadzu) with a CONTR-10 tip (NanoWorld). Fourier transform infrared (FTIR) spectra were acquired in the region of 400-4000 cm^{-1} at a resolution of 4 cm^{-1} and accumulating 32 scans by 640-IR spectrometer (VARIAN) using the KBr pressed disk technique. The X-ray diffraction patterns were investigated with XRD-6000 and XD-3A diffractometer (Shimadzu) using CuKα radiation, with 40 kV and 40 mA, at 0.02° scan rate (in 2θ) with step of 10 s per point.

The C, N and O element contents were determined by the element analysis (CHN SO PE 2400 series II, PerkinElmer). The chemical states of the sample's surface were recorded on an X-ray photoelectron spectroscopy (K-Alpha, Thermo Scientific) with Al Kα line (hν =1286.6 eV) and a pass energy set at 200 eV. The broad and narrow scans were fit using Shirley backgrounds. Diffuse reflectance spectroscopy was analyzed using a UV-Vis spectrometer with wavelenght range of 240-850 nm.

3. Results and discussions

3.1 Characterization

The samples morphologies and microstructures were observed by SEM images. The CN/U displayed micrometer cloud-flake particles, and CN/M showed a flower-like morphology (**Fig. S3**). On the other hand, the CN/CU material texture revealed craked-surfaced carbon spheres with holes in the smooth area. In contrast, the CN/CM matrix presented undefined holes on the fracture and irregular protrusions as observed by Prola et al (**Fig. 1**) [36].

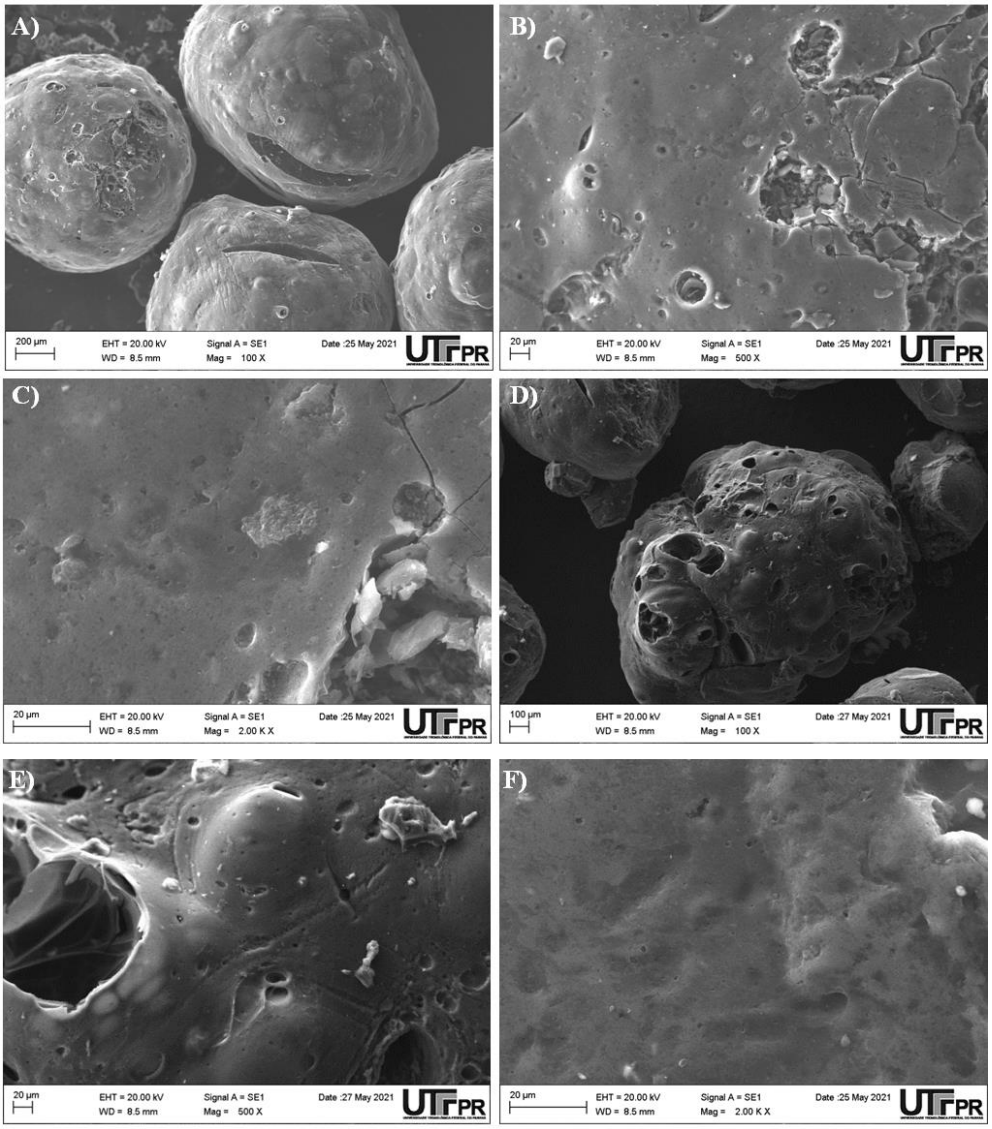

Fig. 1. SEM images of (a-c) CN/CU and (d-e) CN/CU carbon microspheres at different magnitudes.

3D AFM topographic maps for carbon microspheres further confirmed the surface roughness. The obtained CN/CU reveals a smooth surface, while the CN/CM surface shows more irregularities and high surface roughness. Both materials consist of nanometric pores of various depths and widths/nanometer-sized porosity ranging from 6 to 26 nm. An increase in the RMS of the surface roughness and height of grains was noticed for CN/CM material (**Fig. 2**.) [37].

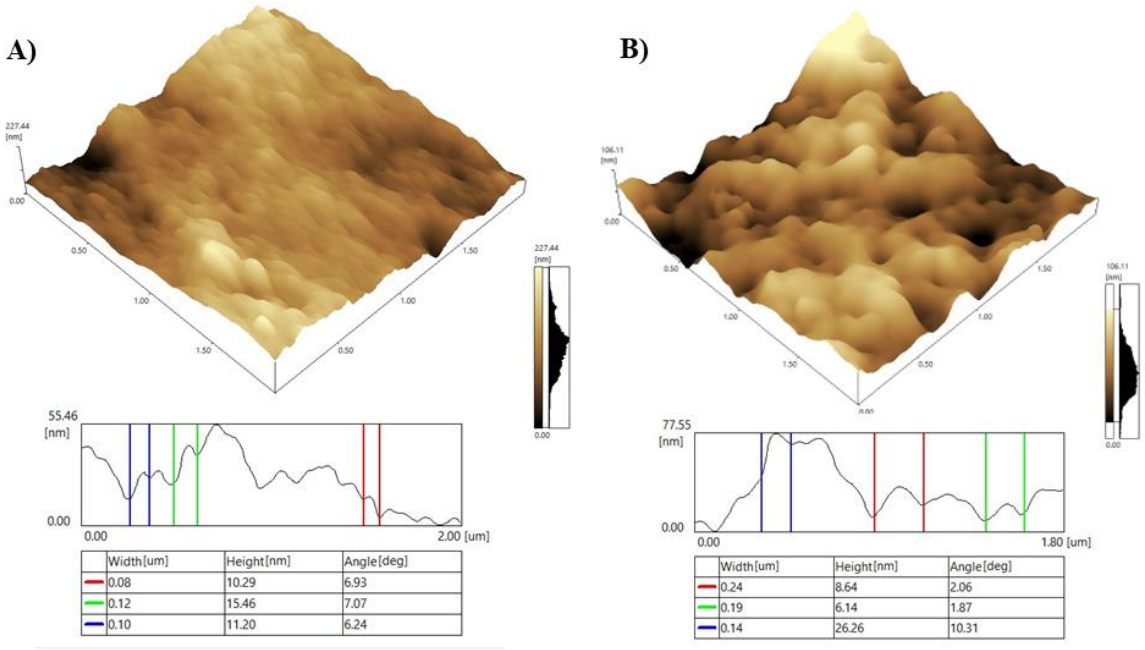

Fig. 2. AFM 3D surface topography for (a) CN/CU and (b) CN/CM carbon microspheres.

The crystallinity of the as-synthesized samples was studied by XRD (**Fig. 3**). As is evident in XRD patterns, two characteristic peaks of g-C_3N_4 structure were present for CN/U and CN/M. The 12.92° peak (100) is associated with the interplanar structural packing of tri-s-triazine units (d=0.675 nm) [38]. The sharp peak at 27.58° relates to the diffraction plane (002) with stacking of the graphitic structure (d=0.325 nm) (JCPDS 87-1526) [25,39]. The carbon microspheres exhibit a peak which is consistent with the pure g-C_3N_4. However, the low intensity of the (100) peak suggests that the introduction of carbon decreased the planar size of the in g-C_3N_4 structure [40,41]. The peak 26.68° (002) corresponds to an increase in the interlayer spaces compared to g-C_3N_4. The intercalation effect of the carbon compounds caused the widened crystal plane spacing, making the g-C_3N_4 less compressed [40,42,43]. Moreover, both g-C_3N_4 melam/dimelem intermediates, or arrangements of these could be formed during the thermal polycondensation which presents low crystallinity [44]. The copolymerization process follows the Schiff base mechanism, which

196 is frequently employed to extend the π-conjugated electronic structures of polymers [45].
197 The reactions are initiated by C-N bonds between carbon from chitosan molecules and the
198 nitrogen from melamine or urea, which partially transforms into melam/melem, dimelam
199 compounds and g-C_3N_4. The g-C_3N_4 derived from urea differs from melamine due to
200 additional mechanism steps that occur under the same operating conditions. At
201 approximately 335°C the structural phase changes from urea to melamine-based products
202 are obtained, followed by further heating to around 390°C, resulting in the formation of tri-
203 s-triazine units through rearrangements of melamine. On the other hand, melamine
204 precursors can be directly pyrolyzed and polymerized to form g-C_3N_4 and two significant
205 intermediates, dimelam and melem, can be produced during the thermal condensation [46].
206 These intermediates are generated at around 350°C and 400°C, respectively, and exhibit a
207 similar crystallographic peak near 25°.The samples obtained from melamine display a peak
208 centered at 27.59° attributed to the incomplete polycondensation of the melamine.
209 Moreover, this characteristic peak suggests that the material possesses enhanced
210 crystallinity with fewer defects and disruptions in its graphitic structure compared to
211 samples prepared from urea precursors [47].

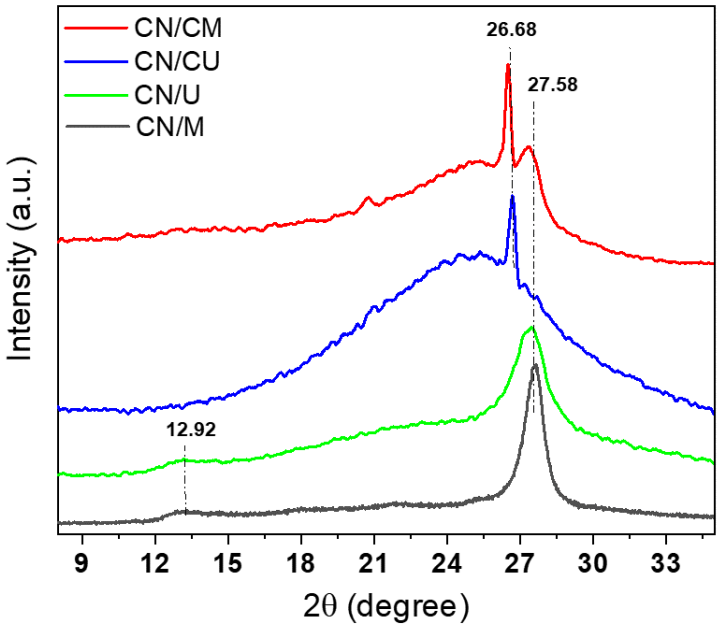

Fig. 3. XRD patterns of the g-C_3N_4 (CN/U and CN/M) and carbon microspheres (CN/CM and CN/CM).

The band gap calculation using the Kubelka-Munk model was performed only for CN/U and CN/M materials (**Fig. 4**) once the carbon microspheres (CN/CU and CN/CM) presented high absorptivity for being black material. The as-prepared samples CN/U and CN/M absorption bands are 384 nm and 374, respectively, related to a blue shift absorption edge (**Fig. 4**). Djoko et al. [24] have already reported a similar observation for g-C_3N_4 prepared at 500 for 3h. According to Liu et al. [48], the band gap values of 3 eV and 3.9 eV are related to intermediate compounds such as melam, melem, or arrangements of these. In addition, several authors estimate that the melem band gap has a value of up to 3.5 eV [49,50]. The intrinsic absorption in the UV light region is related to the transitions between of π - π * states of sp^2 C-N conduction band, the π antibonding orbitals (π*) and valence band from lone pair in the edge N 2p orbitals of the conjugated aromatic ring system [51].

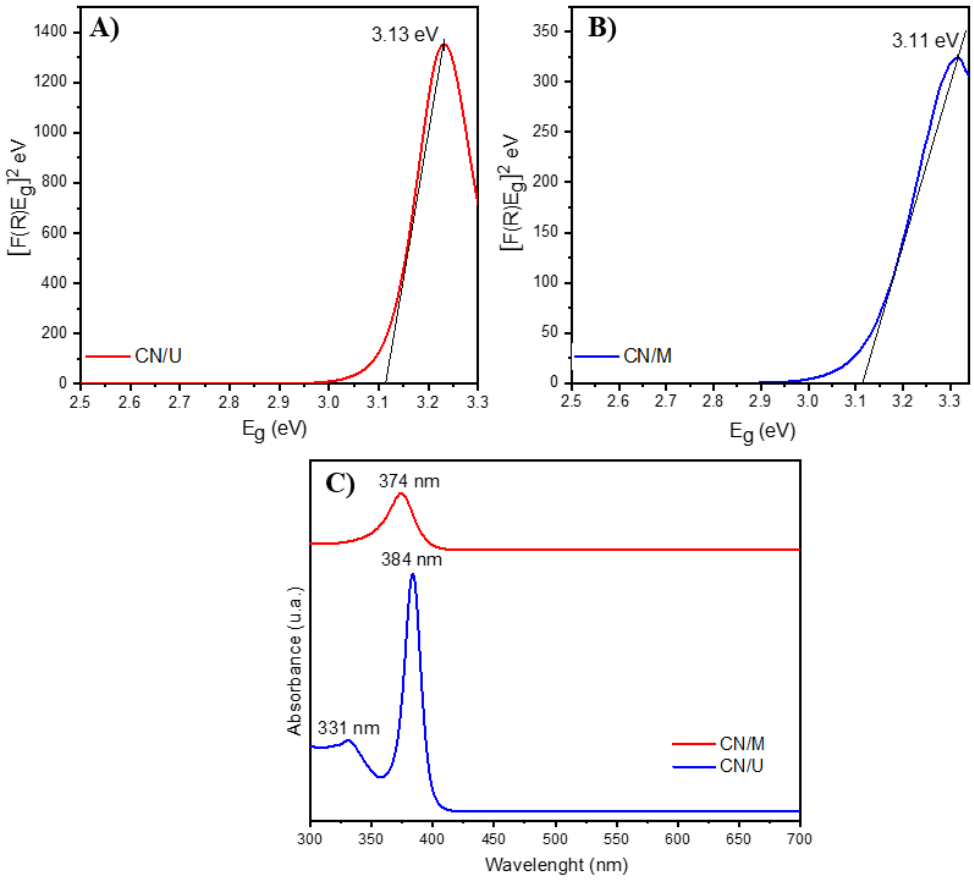

228

229 **Fig. 4.** Band gap calculated by Kubelka-Munk model of CN/U (a) and CN/M (b) materials.

230 UV-Vis absorption spectra of CN/U and CN/M materials (c).

231

232 The FTIR spectra analyzed the carbon microspheres and g-C_3N_4 chemical structure. In **Fig.**

233 **5** can be seen the typical molecular structure of g-C_3N_4 precursors, urea, and melamine,

234 respectively. The broad band in the 3000-3500 cm^{-1} region is attributed to the stretching

235 vibrations of the NH_2 terminal groups [52]. A decrease in the intensity of these peaks

236 indicates the thermal condensation process from urea or melamine to polymeric g-C_3N_4.

237 FT-IR spectrum of CN/U and CN/M display the main characteristic peaks of g-C_3N_4

238 structure that is assigned to triazine units at 802 cm^{-1} and the tri-s-triazine groups (C-N-HC

239 and C=N stretching) at 1200-1620 cm^{-1} [27,39]. The CS introduction altered the periodicity

240 of the peaks in the CN structure. As observed for CN/CU_{bc} and CN/CM_{bc} material, the

bands of O-H groups at 3416 cm^{-1} are related to urea compound in the CS structure. After thermal treatment, for CN/CU and CN/CM samples, the intensity of triazine-related groups significantly decreases with the increase in the carbon content sp^2 C=N-C bonds from N atoms in the g-C_3N_4 and C in the CS [53,54].

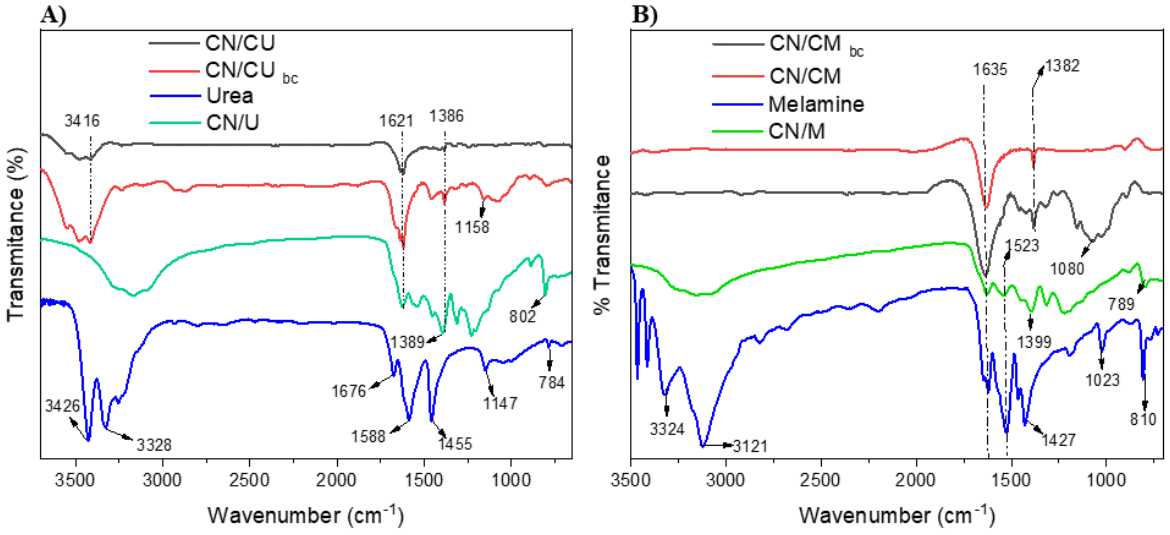

*bc: before carbonization.

Fig. 5. FTIR spectra of the g-C_3N_4 (CN/U and CN/M) and carbon microspheres (CN/CM and CN/CM) from different precursors. (a) Urea. (b) Melamine.

X-ray photoelectron spectroscopy (XPS) presents the chemical states and surface elemental composition of pure g-C_3N_4 and carbon microspheres (**Fig. 6**). The survey spectra indicates that pure CN/U and CN/M samples are essentially composed of C and N. The C 1s spectrum of shows two separated peaks at 287.3 eV indicating the sp^2 C atoms bonded to N in the tris-s-triazine ring (N-C=N) and peak at 284.3 eV related to graphitic carbon (C–C/C=C) [55–57]. The core-level spectra of N 1s can be well-fitted to two peaks at 397.9 eV that correspond to sp^2 hybridized nitrogen in triazine rings (N_2c, C-N=C). The binding energy around 399.7 eV is attributed to the tertiary nitrogen N–$(C)_3$ groups. These assignments of C 1s and N 1s agree with the g-C_3N_4 reported previously Li et al. [58,59].

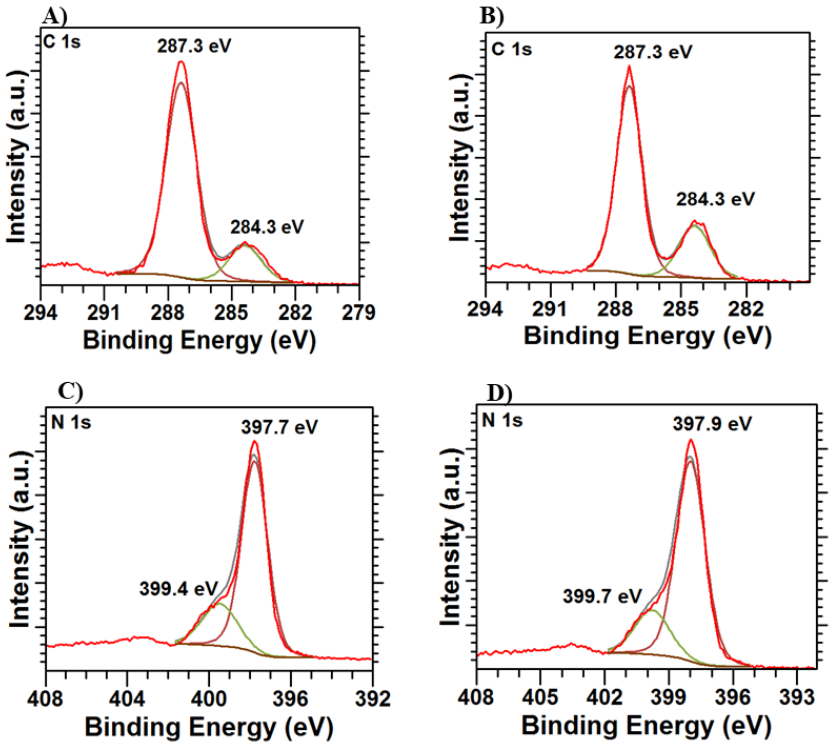

259

260 **Fig. 6.** The deconvoluted individual spectra C1s and N1s of (a,c) CN/U and (b,d) CN/M
261 materials by XPS characterization

262

263 For the carbon microspheres the C, N and O elements are detected in the survey spectra
264 (**Fig 7**). The XPS spectra of C1s, N1s for CN/CM and CN/CU materials indicated similar
265 chemical states for carbon and nitrogen. It should be noticed the intensity of C-C/C=C
266 peak becomes higher than pristine g-C_3N_4 samples, which suggests that the grafted
267 chitosan has been successfully incorporated into g-C_3N_4 structure [40,60].

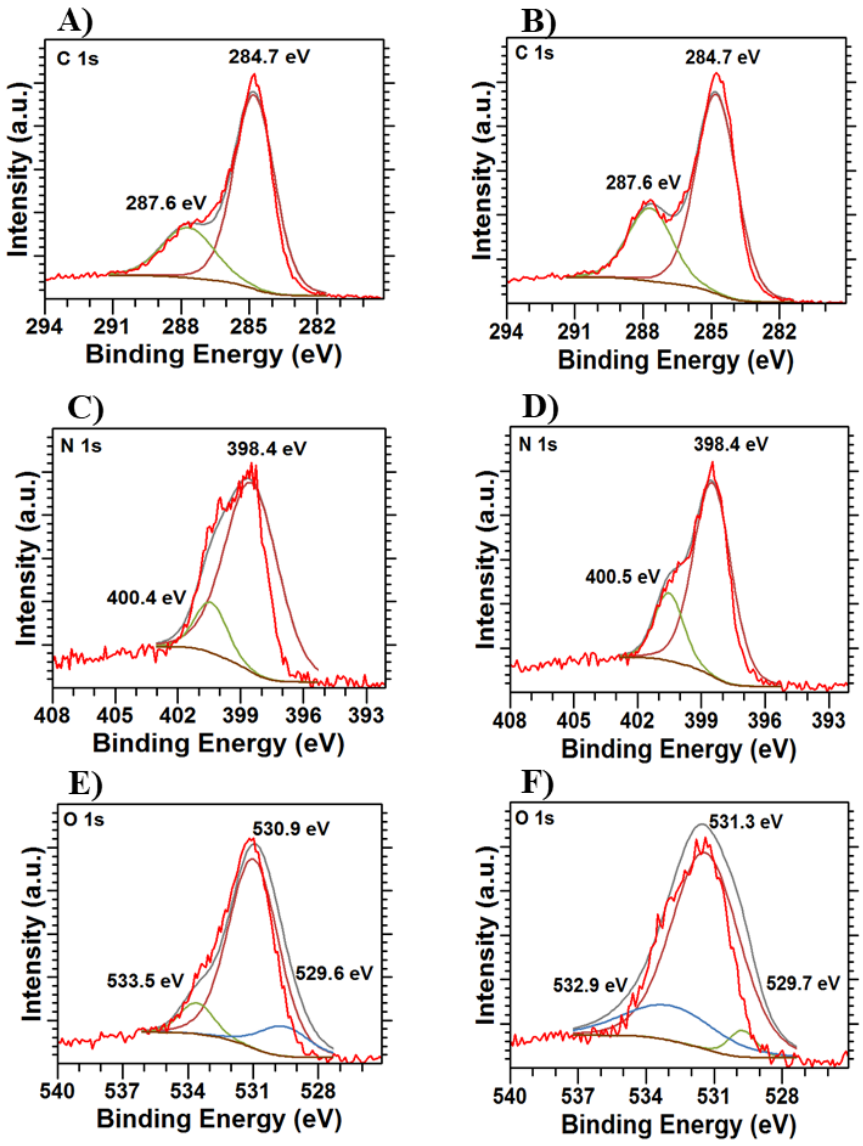

Fig. 7. The deconvoluted individual spectra C1s, N1s and O 1s of (a,c,e) CN/CU and (b,d,f) CN/CM carbon microspheres by XPS characterization.

The calculated atom percentage for C, N and O for all materials is presented in **Table 1**. The C-C to total C atoms peak area increases from 4.75 and 8.96 (CN/U and CN/M) to 31.13 and 30.00 (CN/CU and CN/CM) as a result of the large amount of carbon from chitosan; further, the NHx atom percentage grows, while the N-C=N atom percentage decreases from 50.85 and 54.56 (CN/U and CN/M) to 19.84 and 17.40 (CN/CU and

CN/CM) (**Table S1**). These results show the loss of sp^2 carbon reflects on the appearance of C≡N and an increase of the C-NHx and C-C, suggesting the possibility of molecular bonding between chitosan and g-C_3N_4 [60]. The O 1s observed peaks at 530.8 and 531.3 eV indicating the formation of O-C-N and C-O species via g-C_3N_4 and carbonized chitosan polymer [40,42]. The strong interactions between g-C_3N_4 and carbon can result in efficient charge separation. The peak at 533.6 eV could be attributed to the H_2O adsorbed on the material surface.

Table 1. Surface composition of CN materials and carbon microspheres

Photocatalyst	C (Atom%)	N (Atom %)	O (Atom %)	C/N
CN/U	33.49	66.51		0.5
CN/CU	50.60	26.21	23.19	
CN/M	33.56	66.44		0.5
CN/CM	46.84	16.90	36.26	

* The values in the table were obtained from XPS analysis

The elemental analysis showed C/N ratio of 0.56 that was smaller than the ideal g-C_3N_4 (0.75) [8]. Consequently, incomplete condensation leads to the obtained formation of mainly melam or dimelem intermediates [10]. Besides, compared to CN/U, the N content of CN/CU decreased considerably from 60.9 to 10.93 %, and an increased in the C/N molar ratio. Likewise, the C-O content in chitosan provides g-C_3N_4 with an increased number of oxygen atoms. Elemental analysis (EA) agrees with that of XPS surface analysis (**Table 1**).

3.2 Photocatalytic activity

In this study, the photocatalytic experiments were assessed under three different radiation settings in order to evaluate the material structure and photodegradation response: i) Visible light exposure through the utilization of a suspended white LED lamp; ii) UVA-Vis irradiation involved a suspended (UVA-Vis_S) and solution-immersed (UVA-Vis_I) system employing a Mercury lamp, with radiation filtration by a light bulb.

All solutions were first magnetically stirred in the dark for 15 minutes before irradiation to achieve photocatalyst and dye desorption-desorption equilibrium at pH 5.8. The results showed that the adsorption did not play an essential role in RhB dye removal. The relative concentration profiles C/C_0 for the RhB dye using CN materials and carbon microspheres photocatalysts are shown in **Fig. 8.**

3.2.1 Degradation of RhB by white LED suspended system

The photocatalytic performance of CN and the carbon microspheres were evaluated in comparison to photolysis at room temperature under visible light radiation (**Fig. 8a**). The RhB dye does not degrade in the presence of light (photolysis), confirming its stability and persistence in the environment. The efficiency towards the photodegradation of RhB dye was found to be 29, 9, 21, and 15% in 60 minutes for the CN/U, CN/M, CN/CU and CN/CM, respectively (**Table 2**).

The CN/M degradation efficiency could be explained by formation of g-C_3N and mixed-phase melam/dimelem intermediates that do not absorb visible light radiation from LED lamps. Consequently, the generation of electrons/holes in the CN materials is limited, indicating that the efficiency of g-C_3N_4 is lower than reported in the literature [29,61]. Similar results for g-C_3N_4 using melamine precursor were obtained by Li et al. [62], which the Methyl Orange dye degradation is less than 30% under visible light. Miao et al. also reported that the g-C_3N_4 photocatalyst degraded about 35% of RhB using a 300 W Xe

lamp [63]. On the other hand, the introduction of a carbonaceous matrix through effective molecular bonding between chitosan and g-C_3N_4 resulted in an expressive increase to 16% of RhB dye removal for the CN/CM material, as evidenced by XPS data and the (002) peak 26.68° provided by XRD analysis.

Thus, we can assume that the carbon matrix and the g-C_3N_4 interact synergistically to form two-dimensional planes in which the charge carriers can move freely along the carbon ring structure [10,24] throughout a junction between free N from the heptazine unit and the carbonyl group from the chitosan structure after successive arrangement reactions to form sp^2-hybridized C−N bonds through a Schiff base reaction [64,65].

3.2.2 Degradation of RhB by UVA-Vis immersed and suspended system

The photodegradation experiments were conducted by focusing on the emission profile of the mercury lamp, which has several emission lines present in the ultraviolet and visible region, as well as the absorption of melam/dimelem, and graphitic carbon nitride. In this experiment was used a glass bulb covers the lamp to filter UVC radiation (λ= 254 nm). The UVA-Vis radiation suspended in the solution was also tested to compare the LED system. Experiments without photocatalyst revealed that photolysis using UVA-Vis_S radiation degraded only 3% of RhB (**Table 2**). The efficiency degradation of RhB dye was 27, 11, 14, 12 and 3% in 1 h for CN/U, CN/M, CN/CU, CN/CM, and photolysis, respectively, which indicates the suspended UVA-Vis radiation resulted in comparable to LED system (**Fig. 8b**). For the immersed system (UVA-Vis_I), the CN/U material achieved 99% dye degradation efficiency (**Fig. 8c**). This factor demonstrated the incomplete polycondensation confirmed by a low C/N stoichiometric ratio of 0.56, which resulted in a major melam or dimelem phase [10].

Compared to pristine g-C_3N_4, the CN/U exhibits blue shift absorption to UV, which can be attributed to the intrinsic *band gap* of g-C_3N_4. Therefore, an enhancement in the UV region

absorption reinforced the π - π * transition in π-conjugated structure [51,66]. On the other hand, the CN/M sample showed low RhB degradation of 20%, which could be due to low condensation degree related to melamine peak at 27.58° and a mixed phase in the material structure. Che et al. [63] verified the poor photocatalytic performance of g-C_3N_4 under UV of 22.5% in 120 min of RhB. Therefore, the use of UV lamps for this work is well justified.

Regarding the carbon microspheres, the photocatalytic performance decreased after incorporating carbon chitosan. The poor performance of the materials may be attributed to the so-called shadow effect associated with excess carbonaceous material, which mainly absorbs the incident light limiting the melam/dimelem charge transfer (e-/h+) [67]. Jin et al. obtained the maximum photocatalytic activity optimal concentration of 6 wt% activated carbon in the CN. An increasing the carbonaceous material ratio in the g-C_3N_4 structure leads to a decreased activity originated by the shadow effect [67].

Furthermore, the novelty of this work is based on materials synthesis, which involves the direct mixing of melamine and urea precursors with chitosan, followed by heating to form a new carbon matrix inserted in the graphitic structure.

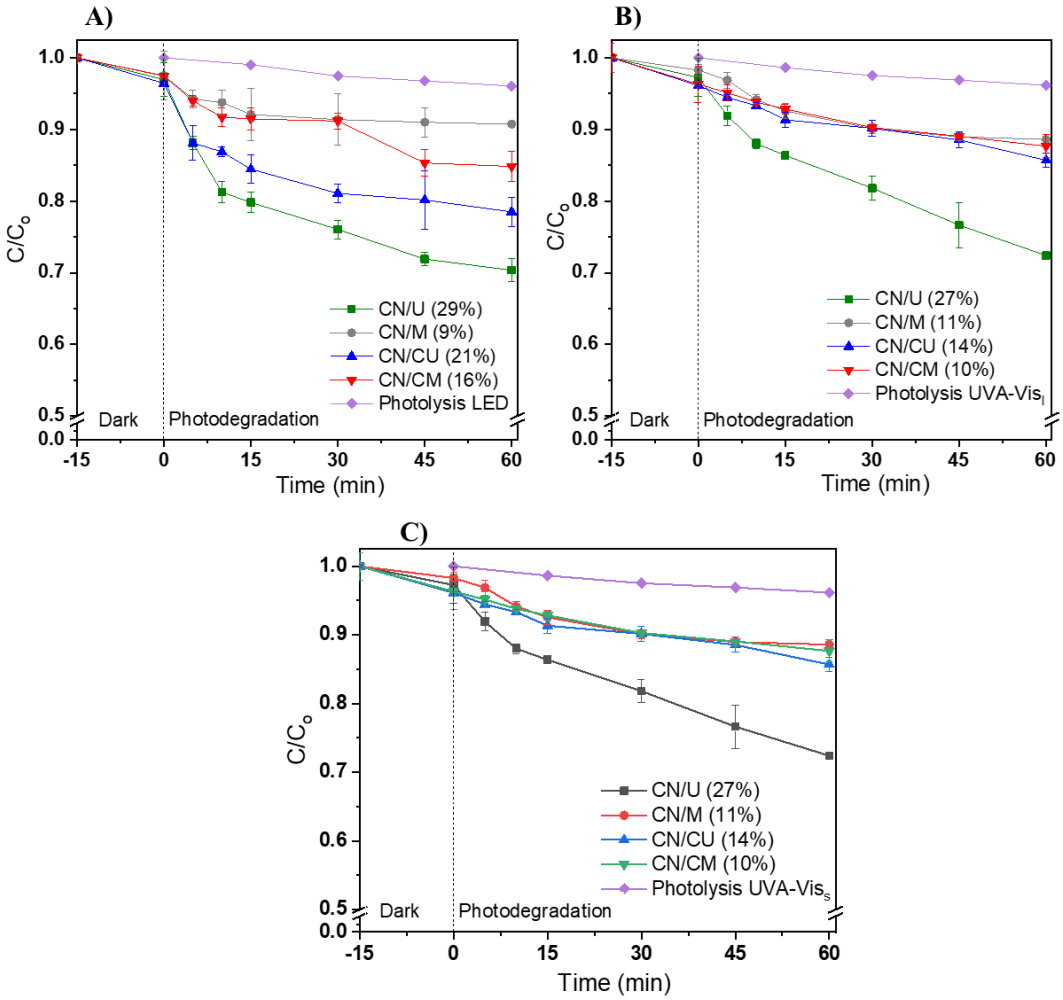

362

363 **Fig. 8.** Photodegradation of RhB on carbon microspheres and CN samples under (A) white
364 LED, (B) UVA-Vis irradiation immersed in the solution and (C) UVA-Vis irradiation
365 suspended. I: immersed; S: suspended. Conditions: C_0 (10 mg L^{-1}, 300 mL); 30 mg of
366 photocatalyst; 60 minutes.

367

368 **Table 2**. Efficiency degradation of carbon microspheres and CN materials for RhB dye by
369 different systems.

Materials (30 mg)	UVA-Visl (%)	White LEDs (%)	UVA-Viss (%)
CN/U	99	29	27
CN/M	20	9	11

CN/CU	16	21	14
CN/CM	15	16	10
Photolysis	7	4	3

*I: immersed; S: Suspended

3.3 Amount of photocatalyst

Fig. 9 illustrates the effects of materials' concentrations on the photocatalytic degradation of RhB. Further increases in the catalyst amount have little impact on the degradation efficiency. The optimal dosage was found to be 0.1 g L^{-1}.

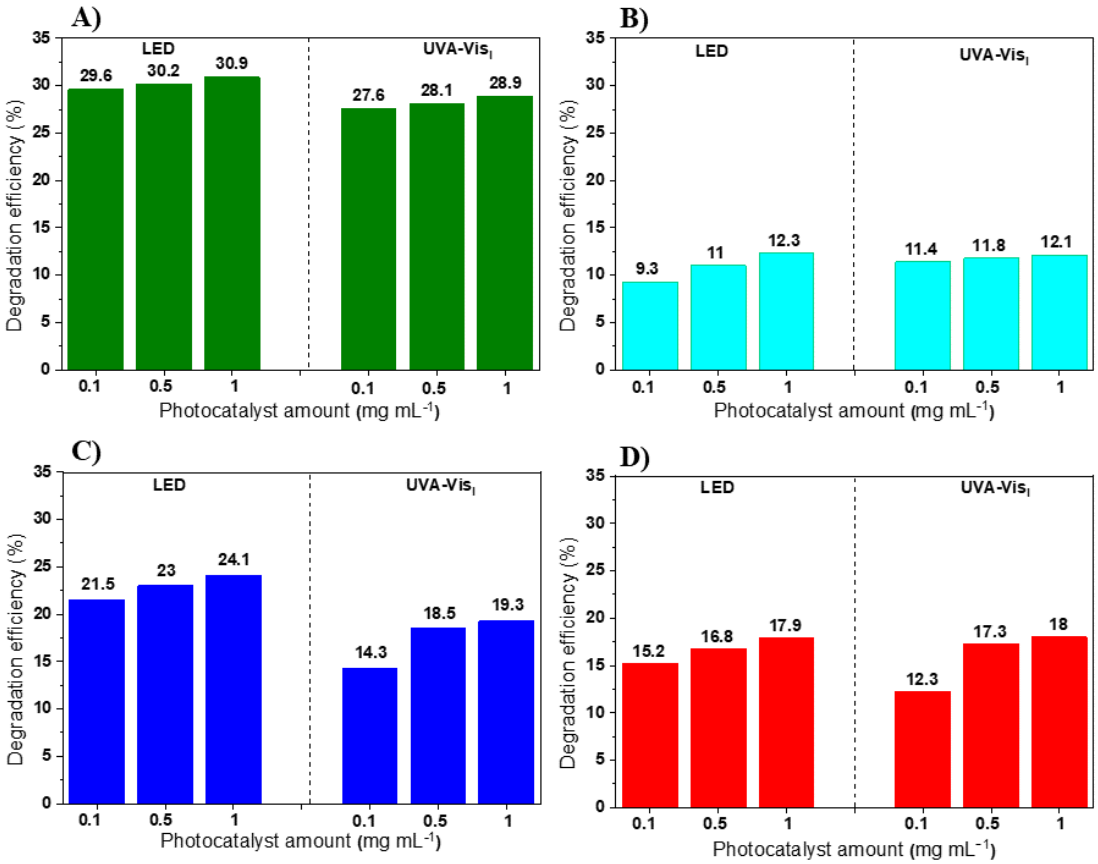

Fig. 9. Effect of photocatalyst amount on RhB photodegradation under white LED and UVA-Vis$_I$ systems. a) CN/U. b) CN/M. c) CN/CU. d) CN/CM. Conditions: C_0 (10 mg L^{-1}, 300 mL); 30 mg of photocatalyst; 60 minutes.

3.4 Materials stability

The stability of the carbon microspheres was tested in three consecutive cycles under illumination by white LED and UVA-Vis_I light under the same conditions described in section 2.3. X-ray diffraction and SEM analysis were used to determine the structural and morphological changes in the materials. The SEM micrographs (**Fig. S4-7**) show no significant structural changes for all samples. It is important to highlight the ease of removing the sphere-shaped photocatalysts from the experimental solution, allowing the photocatalysts to be collected. The crystallographic structure after photocatalysis showed the peaks related to the interplanar packing of tri-s-triazine units and graphitic structure remained after 3 consecutive reuses for CN/U and CN/M. For CN/CM an increased peak intensity in 26.58° using white LED radiation may be associated with decrease of periodic stacking of layers compared to g-C_3N_4. Using UVA-Vis radiation was noticed the loss of usual arrangement of peaks for tri-s-triazine at 27.58° associated to melamine unit [47] **(Fig. 10)**. However, the catalyst's degradation capacity was barely affected throughout the series of experiments. Thus, materials demonstrated all materials great stability and similar photocatalytic performance for RhB dye and could be considered rather stable for reuse **(Fig. 11)**.

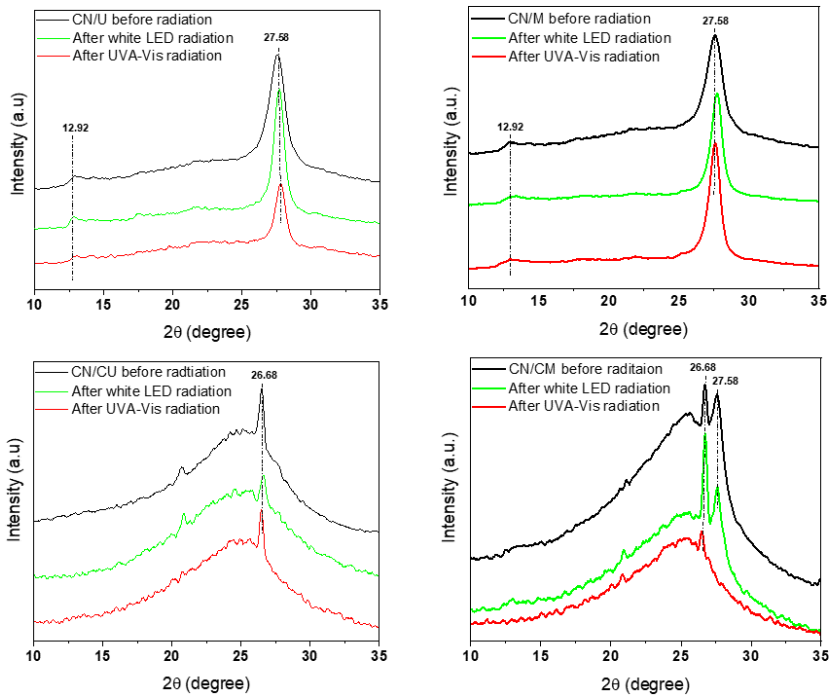

399

400 **Fig. 10.** XRD of the photocatalysts before and after three rounds of photocatalysis.

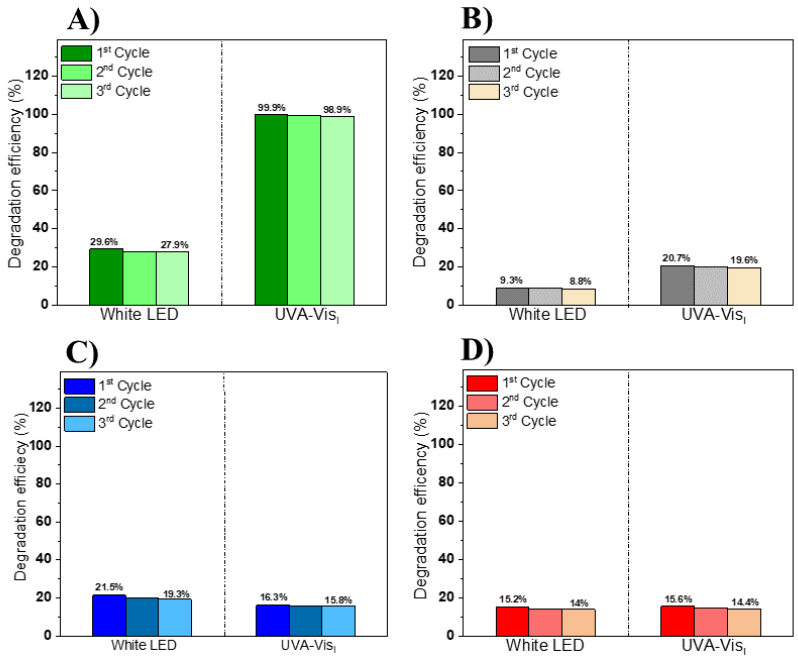

401

402 **Fig. 11.** Stack plot of % degradation of RhB *vs* light radiation for CN/U (a), CN/M (b),

403 CN/CU (c) and CN/CM (d) for all the three cycles.

404

4 Reaction mechanism

Due to the structural composition of melam/dimelem and g-C_3N_4, the degradation mechanism is driven by the UVA-Vis region. Further, the carbon microspheres present higher absorption in the visible region by sp^2-hybridized C−N bonds between the chitosan C-ring and the melam/dimelem units [68]. The incorporation in-plane carbon ring in the CN structure creates crystal defects in the layers that benefit the charge separation on the photocatalyst and improve the photocarrier's transportation synergistically (**Fig. 12**) [63]. The π-conjugated triazine units and the carbon rings may modify the band gap energy to create a new intermediate energy [24,64]. The CN absorbs visible light, which excites the VB electrons and generates holes in the VB. The e^- species are injected into the carbon structure by the π-conjugated system or by C-N bonds and thus accelerate the separation efficiency between photogenerated charges. The holes (h^+) react directly with the RhB molecule, and the e^- reacts with the O_2 presented in the solution to produce $O_2^{\bullet-}$ radical. As observed by Prola et al. [36], the adsorption process does not affect the carbon microspheres removal capacity of RhB dye.

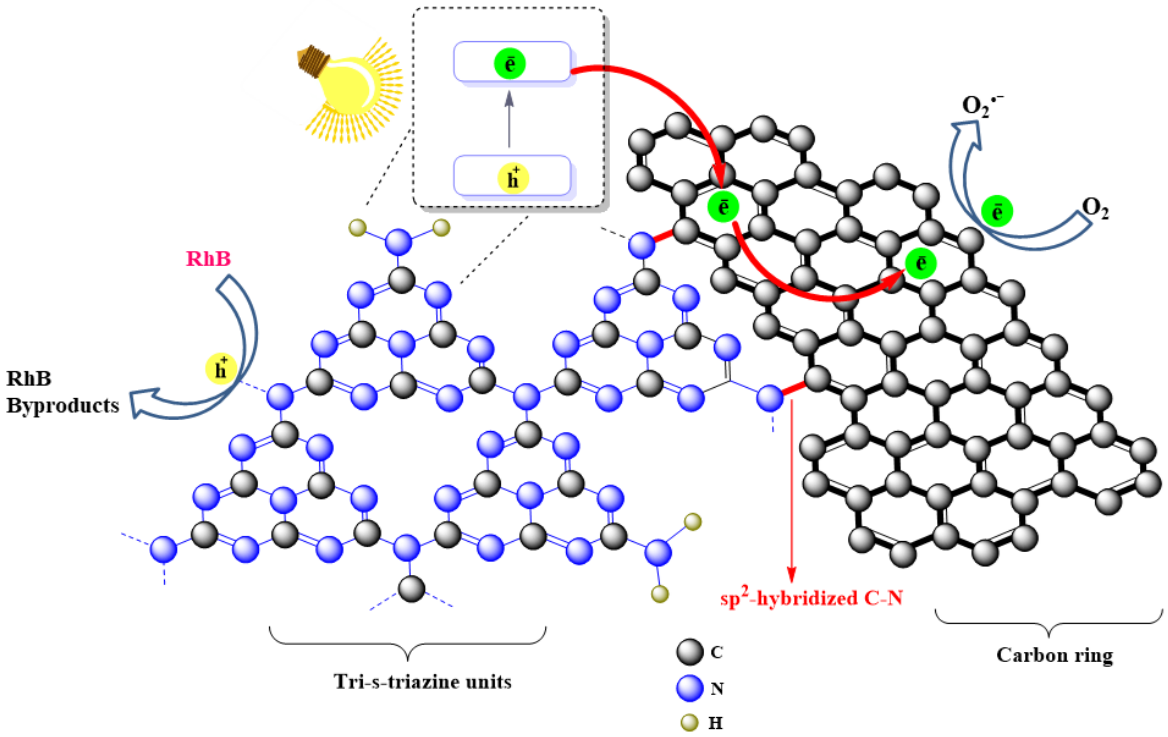

Fig. 12. Schematic mechanism of charge separation and photocatalytic process of carbon microspheres under white LED irradiation.

5 Conclusion

This work presented a new strategy synthesis *in situ* of carbon microspheres and carbon nitride derivates. In summary, the characterization indicated the successful introduction of chitosan in the g-C_3N_4 by a sp^2-hybridized C−N bond between the N from the heptazine structure and the carbonyl group from the chitosan. The UVA-vis experiments and elemental analysis showed C/N ratio of 0.56 indicating a mixed phase of melam/dimelem intermediates. Consequently, the incomplete polycondensation of g-C_3N_4 with carbon matrix results in composite materials with modified band gap energy capable of absorbing radiation in both visible and UVA regions. At the same time, our investigation reveals that an excess of carbonaceous material can hinder the light absorption of CN intermediates

and decrease the composite photocatalytic performance. The low specific surface area and porosity of the carbon microspheres suggest adsorption does not play a leading role in the degradation mechanism. Beside the present work providing a study about the structure and optical properties of CN intermediates combined with the carbonaceous matrix, new investigations related to the photoactivity of melam/dimelem compounds are required.

Acknowledgments

The authors thank the support of the Federal University of Technology-Parana, National Council for Scientific and Technological Development (CNPq), and Coordination for the Improvement of Higher Education Personnel (CAPES). The authors are also grateful to the Multiuser Laboratory of Materials Characterization (CMCM-UTFPR), Multiuser Laboratory of Chemical Analysis (LAMAQ-UTFPR), Materials Chemistry Group at Federal University of Parana (GQM) for the equipment's availability and Surface and Plasma Laboratory (LabPlasma).

Data and code availability

The data that support the findings of this study are available on request from the corresponding author.

References

[1] The United Nations World Water Development Report, Wastewater the Untapped Resource, Paris, 2017.

[2] L.D.T. Prola, F.M. Machado, C.P. Bergmann, F.E. de Souza, C.R. Gally, E.C. Lima, M.A. Adebayo, S.L.P. Dias, T. Calvete, Adsorption of Direct Blue 53 dye from

aqueous solutions by multi-walled carbon nanotubes and activated carbon, J Environ Manage. 130 (2013). https://doi.org/10.1016/j.jenvman.2013.09.003.

[3] F. Rodrigues-Silva, G.P. Masceno, P.P. Panicio, R. Imoski, L.D.T. Prola, C.B. Vidal, C.R. Xavier, W.A. Ramsdorf, F.H. Passig, M.V. de Liz, Removal of micropollutants by UASB reactor and post-treatment by Fenton and photo-Fenton: Matrix effect and toxicity responses, Environ Res. 212 (2022). https://doi.org/10.1016/j.envres.2022.113396.

[4] D. Friedmann, A General Overview of Heterogeneous Photocatalysis as a Remediation Technology for Wastewaters Containing Pharmaceutical Compounds, Water (Basel). 14 (2022) 3588. https://doi.org/10.3390/w14213588.

[5] J. Liu, N. Ma, W. Wu, Q. He, Recent progress on photocatalytic heterostructures with full solar spectral responses, Chemical Engineering Journal. 393 (2020). https://doi.org/10.1016/j.cej.2020.124719.

[6] H. Sepehrmansourie, H. Alamgholiloo, N. Noroozi Pesyan, M.A. Zolfigol, A MOF-on-MOF strategy to construct double Z-scheme heterojunction for high-performance photocatalytic degradation, Appl Catal B. 321 (2023). https://doi.org/10.1016/j.apcatb.2022.122082.

[7] K. Li, W. Zhou, X. Li, Q. Li, S.A.C. Carabineiro, S. Zhang, J. Fan, K. Lv, Synergistic effect of cyano defects and CaCO3 in graphitic carbon nitride nanosheets for efficient visible-light-driven photocatalytic NO removal, J Hazard Mater. 442 (2023). https://doi.org/10.1016/j.jhazmat.2022.130040.

[8] W.J. Ong, L.L. Tan, Y.H. Ng, S.T. Yong, S.P. Chai, Graphitic Carbon Nitride (g-C3N4)-Based Photocatalysts for Artificial Photosynthesis and Environmental Remediation: Are We a Step Closer to Achieving Sustainability?, Chem Rev. 116 (2016) 7159–7329. https://doi.org/10.1021/acs.chemrev.6b00075.

[9] B. Xu, M.B. Ahmed, J.L. Zhou, A. Altaee, G. Xu, M. Wu, Graphitic carbon nitride based nanocomposites for the photocatalysis of organic contaminants under visible irradiation: Progress, limitations and future directions, Science of the Total Environment. 633 (2018) 546–559. https://doi.org/10.1016/j.scitotenv.2018.03.206.

[10] N. Liu, T. Li, Z. Zhao, J. Liu, X. Luo, X. Yuan, K. Luo, K. Luo, J. He, D. Yu, Y. Zhao, From Triazine to Heptazine: Origin of Graphitic Carbon Nitride as a Photocatalyst, ACS Omega. 5 (2020) 12557–12567. https://doi.org/10.1021/acsomega.0c01607.

[11] F.K. Kessler, Y. Zheng, D. Schwarz, C. Merschjann, W. Schnick, X. Wang, M.J. Bojdys, Functional carbon nitride materials-design strategies for electrochemical devices, Nat Rev Mater. 2 (2017). https://doi.org/10.1038/natrevmats.2017.30.

[12] H. Lan, L. Li, H. Liu, X. An, F. Liu, C. Chen, J. Qu, Melem-based derivatives as metal-free photocatalysts for simultaneous reduction of Cr(VI) and degradation of 5-Sulfosalicylic acid, J Colloid Interface Sci. 507 (2017) 162–171. https://doi.org/10.1016/j.jcis.2017.07.099.

[13] S. Chu, C. Wang, J. Feng, Y. Wang, Z. Zou, Melem: A metal-free unit for photocatalytic hydrogen evolution, in: Int J Hydrogen Energy, Elsevier Ltd, 2014: pp. 13519–13526. https://doi.org/10.1016/j.ijhydene.2014.02.052.

[14] X. Li, G. Huang, X. Chen, J. Huang, M. Li, J. Yin, Y. Liang, Y. Yao, Y. Li, A review on graphitic carbon nitride (g-C3N4) based hybrid membranes for water and wastewater treatment, Science of the Total Environment. 792 (2021). https://doi.org/10.1016/j.scitotenv.2021.148462.

[15] J. Chen, S. Fang, Q. Shen, J. Fan, Q. Li, K. Lv, Recent Advances of Doping and Surface Modifying Carbon Nitride with Characterization Techniques, Catalysts. 12 (2022). https://doi.org/10.3390/catal12090962.

[16] Z. Qi, J. Chen, W. Zhou, Y. Li, X. Li, S. Zhang, J. Fan, K. Lv, Synergistic effects of holey nanosheet and sulfur-doping on the photocatalytic activity of carbon nitride towards NO removal, Chemosphere. 316 (2023). https://doi.org/10.1016/j.chemosphere.2023.137813.

[17] G. Li, C. Yang, Q. He, J. Liu, Ag-based photocatalytic heterostructures: Construction and photocatalytic energy conversion application, J Environ Chem Eng. 10 (2022). https://doi.org/10.1016/j.jece.2022.107374.

[18] S. Patnaik, D.P. Sahoo, K. Parida, Recent advances in anion doped g-C3N4 photocatalysts: A review, Carbon N Y. 172 (2021) 682–711. https://doi.org/10.1016/j.carbon.2020.10.073.

[19] D.S. Vavilapalli, R.G. Peri, R.K. Sharma, U.K. Goutam, B. Muthuraaman, M.S. Ramachandra Rao, S. Singh, g-C3N4/Ca2Fe2O5 heterostructures for enhanced photocatalytic degradation of organic effluents under sunlight, Sci Rep. 11 (2021). https://doi.org/10.1038/s41598-021-99020-6.

[20] E. Girija Shankar, M. Aishwarya, A. Khan, A.B.V.K. Kumar, J.S. Yu, Efficient solar light photocatalytic degradation of commercial pharmaceutical drug and dye using rGO-PANI assisted c-ZnO heterojunction nanocomposites, Ceram Int. 47 (2021) 23770–23780. https://doi.org/10.1016/j.ceramint.2021.03.206.

[21] A. Balakrishnan, M. Chinthala, Comprehensive review on advanced reusability of g-C3N4 based photocatalysts for the removal of organic pollutants, Chemosphere. 297 (2022) 134190–134215. https://doi.org/10.1016/j.chemosphere.2022.134190.

[22] Y. Chen, Y. Liu, Z. Ma, G-c3 n4 sensitized by an indoline dye for photocatalytic h2 evolution, Processes. 9 (2021). https://doi.org/10.3390/pr9061055.

[23] Q. Xu, B. Cheng, J. Yu, G. Liu, Making co-condensed amorphous carbon/g-C3N4 composites with improved visible-light photocatalytic H2-production performance

using Pt as cocatalyst, Carbon N Y. 118 (2017) 241–249. https://doi.org/10.1016/j.carbon.2017.03.052.

[24] S.Y. Tameu Djoko, H. Bashiri, E.T. Njoyim, M. Arabameri, S. Djepang, A.K. Tamo, S. Laminsi, M. Tasbihi, M. Schwarze, R. Schomäcker, Urea and green tea like precursors for the preparation of g-C3N4 based carbon nanomaterials (CNMs) composites as photocatalysts for photodegradation of pollutants under UV light irradiation, J Photochem Photobiol A Chem. 398 (2020). https://doi.org/10.1016/j.jphotochem.2020.112596.

[25] C. Li, Z. Sun, X. Li, L. Liu, S. Zheng, Facile fabrication of g-C 3 N 4 / precipitated silica composite with enhanced visible-light photoactivity for the degradation of rhodamine B and Congo red, Advanced Powder Technology. 27 (2016) 2051–2060. https://doi.org/10.1016/j.apt.2016.07.014.

[26] C. Zhao, Q. Yan, S. Wang, P. Dong, L. Zhang, Regenerable g-C 3 N 4 -chitosan beads with enhanced photocatalytic activity and stability, RSC Adv. 8 (2018) 27516–27524. https://doi.org/10.1039/c8ra04293d.

[27] W. Yang, L. Jia, P. Wu, H. Zhai, J. He, C. Liu, W. Jiang, Effect of thermal program on structure–activity relationship of g-C3N4 prepared by urea pyrolysis and its application for controllable production of g-C3N4, J Solid State Chem. 304 (2021) 122545. https://doi.org/10.1016/j.jssc.2021.122545.

[28] H. Sun, F. Guo, J. Pan, W. Huang, K. Wang, W. Shi, One-pot thermal polymerization route to prepare N-deficient modified g-C3N4 for the degradation of tetracycline by the synergistic effect of photocatalysis and persulfate-based advanced oxidation process, Chemical Engineering Journal. 406 (2021) 126844. https://doi.org/10.1016/j.cej.2020.126844.

[29] S. Kokate, S. Gupta, V.G. Kopuri, H. Prakash, Energy efficient photocatalytic activation of peroxymonosulfate by g-C3N4 under 400 nm LED irradiation for degradation of Acid Orange 7, Chemosphere. 287 (2022) 132099. https://doi.org/10.1016/j.chemosphere.2021.132099.

[30] R. Zhang, K. Zeng, A novel flower-like dual Z-scheme BiSI/Bi2WO6/g-C3N4 photocatalyst has excellent photocatalytic activity for the degradation of organic pollutants under visible light, Diam Relat Mater. 115 (2021) 108343. https://doi.org/10.1016/j.diamond.2021.108343.

[31] G. Di, Z. Zhu, Q. Dai, H. Zhang, X. Shen, Y. Qiu, Y. Huang, J. Yu, D. Yin, S. Küppers, Wavelength-dependent effects of carbon quantum dots on the photocatalytic activity of g-C3N4 enabled by LEDs, Chemical Engineering Journal. 379 (2020) 122296. https://doi.org/10.1016/j.cej.2019.122296.

[32] K.M. Reza, A. Kurny, F. Gulshan, Parameters affecting the photocatalytic degradation of dyes using TiO2: a review, Appl Water Sci. 7 (2017) 1569–1578. https://doi.org/10.1007/s13201-015-0367-y.

[33] A. Rana, A. Sudhaik, P. Raizada, A.A.P. Khan, Q. Van Le, A. Singh, R. Selvasembian, A. Nadda, P. Singh, An overview on cellulose-supported semiconductor photocatalysts for water purification, Nanotechnology for Environmental Engineering. 6 (2021) 1–40. https://doi.org/10.1007/s41204-021-00135-y.

[34] S. Li, C. Wang, Y. Liu, Y. Liu, M. Cai, W. Zhao, X. Duan, S-scheme MIL-101(Fe) octahedrons modified Bi2WO6 microspheres for photocatalytic decontamination of Cr(VI) and tetracycline hydrochloride: Synergistic insights, reaction pathways, and toxicity analysis, Chemical Engineering Journal. 455 (2023). https://doi.org/10.1016/j.cej.2022.140943.

[35] C. Liu, Y. Zhang, J. Wu, H. Dai, C. Ma, Q. Zhang, Z. Zou, Ag-Pd alloy decorated ZnIn2S4 microspheres with optimal Schottky barrier height for boosting visible-light-driven hydrogen evolution, J Mater Sci Technol. 114 (2022) 81–89. https://doi.org/10.1016/j.jmst.2021.12.003.

[36] L.D.T. Prola, L. Bach-Toledo, J. Schultz, A.S. Mangrich, P.G. Peralta-Zamora, Synthesis, Characterization, and Synergic Photocatalytic Activity of Amorphous TiO2/Chitosan Carbon Microspheres, J Braz Chem Soc. 31 (2020) 1306–1316. https://doi.org/10.21577/0103-5053.20200016.

[37] T. Katan, R. Kargl, T. Mohan, T. Steindorfer, M. Mozetič, J. Kovač, K. Stana Kleinschek, Solid Phase Peptide Synthesis on Chitosan Thin Films, Biomacromolecules. 23 (2022) 731–742. https://doi.org/10.1021/acs.biomac.1c01155.

[38] H.Y. Xu, L.C. Wu, H. Zhao, L.G. Jin, S.Y. Qi, Synergic Effect between Adsorption and Photocatalysis of Metal-Free g-C3N4 Derived from Different Precursors, PLoS One. 10 (2015). https://doi.org/10.1371/journal.pone.0142616.

[39] J. Wen, J. Xie, X. Chen, X. Li, A review on g-C3N4-based photocatalysts, Appl Surf Sci. 391 (2017) 72–123. https://doi.org/10.1016/j.apsusc.2016.07.030.

[40] Q. Xu, C. Jiang, B. Cheng, J. Yu, Enhanced visible-light photocatalytic H_2-generation activity of carbon/g-C_3N_4 nanocomposites prepared by two-step thermal treatment, Dalton Trans. (2017) 10611–10619. https://doi.org/10.1039/C7DT00629B.

[41] X. Wu, S. Li, B. Wang, J. Liu, M. Yu, From biomass chitin to mesoporous nanosheets assembled loofa sponge-like N-doped carbon/g-C3N4 3D network architectures as ultralow-cost bifunctional oxygen catalysts, Microporous and

Mesoporous Materials. 240 (2017) 216–226. https://doi.org/10.1016/j.micromeso.2016.11.022.

[42] Y. Yang, Z. Bian, Oxygen doping through oxidation causes the main active substance in g-C3N4 photocatalysis to change from holes to singlet oxygen, Science of the Total Environment. 753 (2021) 141908. https://doi.org/10.1016/j.scitotenv.2020.141908.

[43] Y. Gao, F. Hou, S. Hu, B. Wu, Y. Wang, H. Zhang, B. Jiang, H. Fu, Graphene Quantum-Dot-Modified Hexagonal Tubular Carbon Nitride for Visible-Light Photocatalytic Hydrogen Evolution, ChemCatChem. 10 (2018) 1330–1335. https://doi.org/10.1002/cctc.201701823.

[44] B. Rani, A.K. Nayak, N.K. Sahu, Degradation of mixed cationic dye pollutant by metal free melem derivatives and graphitic carbon nitride, Chemosphere. 298 (2022) 134249. https://doi.org/10.1016/j.chemosphere.2022.134249.

[45] X. Fan, L. Zhang, M. Wang, W. Huang, Y. Zhou, M. Li, R. Cheng, J. Shi, Constructing carbon-nitride-based copolymers via Schiff base chemistry for visible-light photocatalytic hydrogen evolution, Appl Catal B. 182 (2016) 68–73. https://doi.org/10.1016/j.apcatb.2015.09.006.

[46] W.J. Ong, L.L. Tan, Y.H. Ng, S.T. Yong, S.P. Chai, Graphitic Carbon Nitride (g-C3N4)-Based Photocatalysts for Artificial Photosynthesis and Environmental Remediation: Are We a Step Closer to Achieving Sustainability?, Chem Rev. 116 (2016) 7159–7329. https://doi.org/10.1021/acs.chemrev.6b00075.

[47] H.Y. Xu, L.C. Wu, H. Zhao, L.G. Jin, S.Y. Qi, Synergic Effect between Adsorption and Photocatalysis of Metal-Free g-C3N4 Derived from Different Precursors, PLoS One. 10 (2015). https://doi.org/10.1371/journal.pone.0142616.

628 [48] S. Liu, H. Sun, K. O'Donnell, H.M. Ang, M.O. Tade, S. Wang, Metal-free melem/g-
629 C3N4 hybrid photocatalysts for water treatment, J Colloid Interface Sci. 464 (2016)
630 10–17. https://doi.org/10.1016/j.jcis.2015.11.003.
631 [49] A. Alaghmandfard, K. Ghandi, A Comprehensive Review of Graphitic Carbon
632 Nitride (g-C3N4)–Metal Oxide-Based Nanocomposites: Potential for Photocatalysis
633 and Sensing, Nanomaterials. 12 (2022). https://doi.org/10.3390/nano12020294.
634 [50] A. Mishra, A. Mehta, S. Basu, N.P. Shetti, K.R. Reddy, T.M. Aminabhavi,
635 Graphitic carbon nitride (g–C3N4)–based metal-free photocatalysts for water
636 splitting: A review, Carbon N Y. 149 (2019) 693–721.
637 https://doi.org/10.1016/j.carbon.2019.04.104.
638 [51] X. Li, J. Bai, J. Li, C. Li, X. Zhong, S. Deng, The effect of n-π electronic transitions
639 on the N2 photofixation ability of carbon self-doped honeycomb-like g-C3N4
640 prepared: Via microwave treatment, RSC Adv. 10 (2020) 7019–7025.
641 https://doi.org/10.1039/d0ra00101e.
642 [52] G. Madhurambal, M. Mariappan, S.C. Mojumdar, Thermal, UV and FTIR spectral
643 studies of urea-thiourea zinc chloride single crystal, J Therm Anal Calorim. 100
644 (2010) 763–768. https://doi.org/10.1007/s10973-010-0758-0.
645 [53] K. Li, X. Xie, W. De Zhang, Photocatalysts based on g-C3N4-encapsulating carbon
646 spheres with high visible light activity for photocatalytic hydrogen evolution,
647 Carbon N Y. 110 (2016) 356–366. https://doi.org/10.1016/j.carbon.2016.09.039.
648 [54] X. Chen, D.H. Kuo, D. Lu, Nanonization of g-C3N4 with the assistance of activated
649 carbon for improved visible light photocatalysis, RSC Adv. 6 (2016) 66814–66821.
650 https://doi.org/10.1039/c6ra10357j.
651 [55] D. Briggs, X-ray photoelectron spectroscopy (XPS), Handbook of Adhesion:
652 Second Edition. (2005) 621–622. https://doi.org/10.1002/0470014229.ch22.

[56] H. Fattahimoghaddam, T. Mahvelati-Shamsabadi, B.K. Lee, Efficient Photodegradation of Rhodamine B and Tetracycline over Robust and Green g-C3N4 Nanostructures: Supramolecular Design, J Hazard Mater. 403 (2021) 123703. https://doi.org/10.1016/j.jhazmat.2020.123703.

[57] J. Luo, Y. Liu, C. Fan, L. Tang, S. Yang, M. Liu, M. Wang, C. Feng, X. Ouyang, L. Wang, L. Xu, J. Wang, M. Yan, Direct Attack and Indirect Transfer Mechanisms Dominated by Reactive Oxygen Species for Photocatalytic H2O2Production on g-C3N4Possessing Nitrogen Vacancies, ACS Catal. (2021) 11440–11450. https://doi.org/10.1021/acscatal.1c03103.

[58] K. Li, Z. Huang, X. Zeng, B. Huang, S. Gao, J. Lu, Synergetic Effect of Ti $^{3+}$ and Oxygen Doping on Enhancing Photoelectrochemical and Photocatalytic Properties of TiO $_2$ /g-C $_3$ N $_4$ Heterojunctions, ACS Appl Mater Interfaces. 9 (2017) 11577–11586. https://doi.org/10.1021/acsami.6b16191.

[59] C. Saka, Facile fabrication of P-doped g-C3N4 particles with nitrogen vacancies for efficient dehydrogenation of sodium borohydride methanolysis, Fuel. 313 (2022) 122688. https://doi.org/10.1016/j.fuel.2021.122688.

[60] Y. Lin, L. Wang, Y. Yu, X. Zhang, Y. Yang, W. Guo, R. Zhang, Y. Zhai, Y. Liu, Construction of molecularly doped and cyano defects co-modified graphitic carbon nitride for the efficient photocatalytic degradation of tetracycline hydrochloride, New Journal of Chemistry. 45 (2021) 18598–18608. https://doi.org/10.1039/d1nj03602e.

[61] L. Shi, L. Yao, W. Si, One step to prepare CNTs modified porous g-C3N4 with excellent visible-light photocatalytic performance, Journal of Materials Science: Materials in Electronics. 30 (2019) 1714–1723. https://doi.org/10.1007/s10854-018-0444-8.

678 [62] H. Li, G. Huang, H. Xu, Z. Yang, X. Xu, J. Li, A. Qu, Y. Chen, Enhancing
679 photodegradation activity of g-C3N4 via decorating with S-doped carbon nitride
680 quantum dots by in situ polymerization, J Solid State Chem. 292 (2020) 121705.
681 https://doi.org/10.1016/j.jssc.2020.121705.
682 [63] J. Miao, G. Xu, J. Liu, J. Lv, Y. Wu, Synthesis and photocatalytic performance of g-
683 C3N4 nanosheets via liquid phase stripping, J Solid State Chem. 246 (2017) 186–
684 193. https://doi.org/10.1016/j.jssc.2016.11.028.
685 [64] W. Che, W. Cheng, T. Yao, F. Tang, W. Liu, H. Su, Y. Huang, Q. Liu, J. Liu, F. Hu,
686 Z. Pan, Z. Sun, S. Wei, Fast Photoelectron Transfer in (Cring)-C3N4Plane
687 Heterostructural Nanosheets for Overall Water Splitting, J Am Chem Soc. 139
688 (2017) 3021–3026. https://doi.org/10.1021/jacs.6b11878.
689 [65] X. Fan, L. Zhang, M. Wang, W. Huang, Y. Zhou, M. Li, R. Cheng, J. Shi,
690 Constructing carbon-nitride-based copolymers via Schiff base chemistry for visible-
691 light photocatalytic hydrogen evolution, Appl Catal B. 182 (2016) 68–73.
692 https://doi.org/10.1016/j.apcatb.2015.09.006.
693 [66] X. Yang, F. Qian, G. Zou, M. Li, J. Lu, Y. Li, M. Bao, Facile fabrication of
694 acidified g-C3N4/g-C3N4 hybrids with enhanced photocatalysis performance under
695 visible light irradiation, Appl Catal B. 193 (2016) 22–35.
696 https://doi.org/10.1016/j.apcatb.2016.03.060.
697 [67] Z. Jin, J. Chen, S. Huang, J. Wu, Q. Zhang, W. Zhang, Y.J. Zeng, S. Ruan, T. Ohno,
698 A facile approach to fabricating carbonaceous material/g-C3N4 composites with
699 superior photocatalytic activity, Catal Today. 315 (2018) 149–154.
700 https://doi.org/10.1016/j.cattod.2018.03.012.
701 [68] W. Che, W. Cheng, T. Yao, F. Tang, W. Liu, H. Su, Y. Huang, Q. Liu, J. Liu, F. Hu,
702 Z. Pan, Z. Sun, S. Wei, Fast Photoelectron Transfer in (Cring)-C3N4 Plane

Heterostructural Nanosheets for Overall Water Splitting, J Am Chem Soc. 139 (2017) 3021–3026. https://doi.org/10.1021/jacs.6b11878.